Underground, Incrementally Deployed Magneto-Inductive 3-D Positioning Network

Traian E. Abrudan, *Member, IEEE,* Zhuoling Xiao, *Student Member, IEEE,* Andrew Markham, and Niki Trigoni
Department of Computer Science, University of Oxford
E-mails: firstname.lastname@cs.ox.ac.uk

***Abstract*—Underground mines are characterized by a network of intersecting tunnels and sharp turns, an environment which is particularly challenging for RF-based positioning systems due to extreme multipath, non-line-of-sight propagation and poor anchor geometry. Such systems typically require a dense grid of devices to enable 3-D positioning. Moreover, the precise position of each anchor node needs to be precisely surveyed, a particularly challenging task in underground environments. Magneto-inductive positioning, which provides 3-D position and orientation from a single transmitter and penetrates thick layers of soil and rock without loss, is a more promising approach, but so far has only been investigated in simple point-to-point contexts. In this paper, we develop a novel magneto-inductive positioning approach to cover an extended underground 3-D space with unknown geometry using a rapidly deployable anchor network. Key to our approach is that the position of only a *single* anchor needs to be accurately surveyed – the positions of all secondary anchors are determined using an iterative refinement process using measurements obtained from receivers within the network. This avoids the particularly challenging and time intensive task in an underground environment of accurately surveying the positions of all the transmitters. We also demonstrate how measurements obtained from multiple transmitters can be fused to improve localization accuracy. We validate the proposed approach in a man-made cave, and show that with a portable system that took 5 minutes to deploy, we were able to provide accurate through-the-earth location capability to nodes placed along a suite of tunnels.**

***Index Terms*—Underground, Magneto-inductive, Localization**

I. Introduction

Underground mines, characterized by a network of intersecting tunnels, are a dangerous working environment where people and machinery operate in close proximity. Working conditions are often hazardous due to the unstable terrain, high humidity, low visibility, poor ventilation, flammable and toxic gases, and corrosive water and dust [1]. In spite of strict work safety regulations, the risk of fatal accidents remains substantial, and accidents such as explosion, tunnel collapse and flooding often result in many casualties. One major factor which affects work safety is the lack of a reliable underground positioning system. Such a system could greatly improve mine operations by maintaining safe distances between plant equipment and workers and by logging the most recent location of each worker in the tunnel system. Accurate location is also important for optimizing operations, helping to reduce running costs. One area which has yet to be sufficiently explored is the challenge of providing positioning for a team of rescuers, similar to the way that GPS has revolutionized terrestrial rescue operations. The main challenge with rescue applications is the fact that a permanent infrastructure cannot be relied on but must be incrementally deployed.

Accurate localization may be obtained by using a hand-held laser scanner [2], but the device is too bulky to be carried by the user for long periods of time spent under the ground. Moreover, such devices are prohibitively expensive to be used by large teams of workers [2]. Conventional localization solutions that have been widely used indoors are cheaper, and have been adapted to underground scenarios. They usually rely on radio-frequency (RF) techniques, such as ultra-wideband [3]–[6] or ZigBee [1], [7] enabled wireless sensor networks, and WiFi [8]. However, the RF-based techniques face serious challenges such as extreme path-loss, non-line-of-sight propagation, multipath fading, ambient noise, ionized air, and the waveguide effect [1]. Most limiting is the requirement of good geometry between anchor nodes, with signals from at least four non-colocated anchors to provide range-based positioning in 3-D. Moreover, geometry has a high impact on the network connectivity and energy consumption [9]. It is extremely difficult to achieve a good geometry for RF positioning systems in mines, where tunnels impose strong (typically linear) geometric constraints, and block line-of-sight travel. This leads to severely degraded positioning accuracy, precluding the use of RF based systems for robust and precise positioning.

Magneto-inductive (MI) positioning, on the other hand, does not rely on a propagating wave, but rather establishes a quasi-static field. As the relative magnetic permeability of most materials in an underground environment is close to unity [10], a low frequency (up to a few kilohertz) field can propagate without loss, multipath or fading. This makes MI eminently suitable for underground conditions that correspond to RF non-line-of-sight. However, most work to date has focused on point-to-point positioning in indoor environments [11]–[14]. In this work, we consider, for the first time, how a network of 3-D MI transmitters can be used to provide robust 3-D underground positioning, even when there is no RF line-of-sight between transmitters and receivers. In the proposed system, all TXs and RXs are placed underground, no survey is required, and two TXs are sufficient to determine the RX 3-D position and orientation.

In this work, we consider the problem of localization with a

The authors would like to thank EPSRC for funding this research (Grant ref. EP/L00416X/1 Digital Personhood: Being There: Humans and Robots in Public Spaces (HARPS)).

network of MI transmitters. In particular, we address the key challenge of providing a rapidly deployable positioning system that requires no surveying or precise anchor positioning. This is in stark contrast to existing positioning algorithms which assume that the anchor positions are known accurately which is extremely difficult, time-consuming and expensive to achieve in the underground environment. For the presented system it is only necessary that the position of a *single* anchor is known - there are no other constraints on the positions and orientations of the rest of the deployed infrastructure, other than to maintain coverage. The algorithms presented determine the position of these secondary anchors, using measurements from receivers within range of two or more transmitters. Thus, no additional effort is required to precisely determine the positions and orientations of these additional anchors, a very desirable property of a rapidly deployable localization system. An application in particular that would benefit from such a system is underground rescue, where it is necessary to keep track of the locations of a team of rescue personnel. In such a scenario, the time taken to survey and maintain positioning slows down the entire operation, which in time-critical emergencies could be the difference between a successful rescue or a fatality.

The major contributions of this work are as follows:

1) The system design of a rapidly deployable 3-D magneto-inductive positioning network.
2) A technique for estimating the positions of secondary anchors, bootstrapped from the single surveyed reference anchor.
3) Using *a single anchor node*, we propose a calibration algorithm that iteratively refines the positions and orientations of both receivers and secondary anchors.
4) A fusion algorithm to reduce position and orientation errors from multiple anchors.
5) Proof-of-concept experimental results using real-world data collected in a man-made cave showing sub-meter accuracy in 3-D.

The remainder of the paper is organized as follows. In Section II, we describe the principles of mageto-inductive localization using a single transmitter-receiver pair, whereas in Section III, we introduce a multi-transmitter maximum likelihood estimation algorithm. In Section IV, we present the architecture of the proposed magneto-inductive network. The network deployment algorithm is formulated in mathematical terms in Section V. In Section VI, we evaluate the system performance using real-world data that are collected in a man-made cave. In Section VII, we provide a survey of the related work. Section VIII concludes the paper.

II. Principles of Magneto-Inductive Positioning

In this section, we turn to the fundamental physics that explain how a single magnetic vector source can be used to find the position and orientation of a vector sensor in 3-D. In Section II-A, we address the behavior of very low frequency (VLF) magnetic fields under the ground, and show that the magnetic dipole model is applicable to most natural underground materials. In Section II-B, we introduce the magnetic channel model used to estimated the 3-D position and orientation, which are later addressed in II-C.

A. The Underground Magneto-Inductive Transmission Medium

In free-space, the very low frequency magnetic field can be predicted using the magnetic dipole equations [15], [16]. In this section, we show that the dipole equations can still be applied in most underground environments under the assumption that frequency is sufficiently low. There are two key material properties that undermine the validity of the dipole model: *magnetic permeability* and *electrical conductivity*. These will be addressed next, followed by a summary that provides attenuation figures for the most common underground materials.

1) On Magnetic Permeability: Magnetic materials typically possess different permeability values compared to free-space, thus changing the direction of the incident vector field at the earth-air interface, and invalidating the dipole equations. However, Telford *et al.* [10] address in detail the magnetism of rocks and minerals showing that the vast majority of rocks are non-magnetic, and that the magnetically important minerals are surprisingly few in number [10, Sec. 3.3.5]. Except for some iron and titanium-based compounds, such as magnetite, pyrrhotite and titanomagnetite, all the other minerals have relative magnetic permeability very close to one. In conclusion, since most soils in nature do not contain massive amounts of such minerals in high concentrations, we can safely assume that the relative permeability of most underground environments is close to one. The same assumption was used in [17] for the magneto-inductive communications.

2) On Electric Conductivity: Conductivity gives rise to eddy currents that produce an out-of-phase secondary field [18]. This field superimposes with the primary field, thus distorting the dipole field shape. As a result, the field magnitude decays fast through the material. This decay is associated with the skin effect [19]. However, the conductivity of most underground materials is sufficiently low, such that eddy currents can be ignored at very low frequencies [18], [19]. For example, for the 2.5 KHz carrier used in this paper, the skin depth (defined as the distance at which the signal attenuates by $1/e$, i.e., approx. 8.6 dB) exceeds few tens of meters for the vast majority of rocks and minerals, as shown in Section II-A3. Our through-the-earth experiments carried out in a man-made cave also confirm that the free-space dipole equations hold with high fidelity. By contrast, high frequency radio waves experience extreme attenuation through the ground, as well as distortion due to reflections.

3) Attenuation of VLF Magnetic Fields Underground: In free-space, the magnitude of the VLF decays more rapidly compared to the high-frequency radio waves (60 dB/decade vs. 20 dB/decade), which calls for a very sensitive RX (or a higher TX power). This challenge also strengthens the motivation for using multi-hop networks, such as the one we are proposed in this paper. However, in other materials, conductivity plays an important role, and causes the RF waves undergo extreme attenuation, much higher than VLF. For other materials, the operation range is related to the skin depth. At

(a) Rocks, sediments and water	Skin depth [m]	
	2.5 KHz	10 MHz
Ice, Petroleum, Siltstone (coarse grain), Gneiss (various), Dacite, Siltstone	$\geq$1000	$\geq$112.67
Hornfels, Granite, Siltstone, Conglomerates, Olivine norite, Gabbro, Mica, Slates (various), Dolomite, Serpentine, Andesite, Marble, Soil waters, Lavas	$\geq$100	$\geq$1.77
Limestones, Meteoric waters, Rock salt, Consolidaled shales, Diabase (various), Schists (calcareous and mica), Surface waters (sediments), Argillites, Basalt, Gypsum, Lignite, Natural waters (ign. Rocks), Oil sands, Marls, Clays, Sea water, Sandstones	$\geq$10	$\geq$ 0.15
Bitum. Coal, Surface waters, Anthracite	0.31–4911.6	0.005–2665

(b) Minerals and ores	Skin depth [m]	
	2.5 KHz	10 MHz
Calcite, Sylvite, Quartz, Anhydrite	$\geq$1000	$\geq$ 1000
Limonite, Bauxite, Siderite, Rutile, Diamond, Sphalerite, Chromite	$\geq$10	$\geq$0.16
Hematite, Cassiterite, Stannite, Pyrite, Cuprite, Magnetite, Ilmenite, Pyrolusite, Titanomagnetite	0.05–$25.9{\cdot}10^4$	0.0008–$25.9{\cdot}10^4$
Chalcocite, Bornite, Graphite, Pyrrhotite, Chalcopyrite, Covellite	$\leq$7.79	$\leq$0.12

TABLE I
SKIN DEPTH FOR DIFFERENT ROCKS (TOP) AND MINERALS (BOTTOM) AT TWO DIFFERENT FREQUENCIES: 2.5 KHZ AND 10 MHZ (SORTED IN DESCENDING ORDER, BY MINIMUM VALUE).

the 2500 Hz operation frequency, the skin depth values exceed few tens of meters for most natural materials, whereas for higher frequencies (e.g. already at 10 MHz) the skin depth diminishes considerably. In order to quantify the penetration capabilities of the field, in Table I, we provide values of the skin depth for most common underground materials. We used the general expression for the skin depth as a function of frequency, derived by [20]. We used the electric conductivity, dielectric constant, and magnetic permeability ranges provided in [10], [21] for the most common underground materials, and for different temperature ranges and water content. Table I(a) shows that the 2500 Hz magnetic field penetrates deeply into most rocks, sediments and water, except for some highly conductive coals, and heavily mineralized waters (electrolytes). The same is valid for most common minerals and ores, except for a few highly conductive sulfides of metals and graphite, as shown in Table I(b).

For comparison, we also included the skin depth values corresponding to a higher frequency (10 MHz) that is used for MI communication in order to provide higher bandwidth (see e.g. [17]). The 10 MHz frequency magnetic field is unable to penetrate deeply into most rocks and minerals. By contrast, the superior penetration capabilities of the VLF are obvious, since the frequency is 4 orders of magnitude lower. In [19], it was shown that accurate localization can be achieved even beyond one skin depth, by exploiting the geometric properties of the magnetic fields, at the cost of using at least three transmitters, which would increase the infrastructure costs. More sophisticated models for conductive media have also been proposed in the literature, such as homogeneous earth model [18], [19], stratified earth model [22], and image theory model [23] in highly distorted environments. Channel models for MI communications have been proposed in the literature (e.g. in [17]), but in order to achieve large communication bandwidth, the operation frequency is several orders of magnitude higher than in our system (10 MHz vs. 2.5 KHz in e.g. [17]). This leads to completely different penetration capabilities of the corresponding fields, and to a much more complicated channel model that must account for the complex-values impedances. By contrast, our system is extremely narrowband (few tens of Hz), and the the imaginary part of the complex impedance vanishes. In addition, the higher frequencies experience very high attenuation due to the skin effect. Table I shows that by using VLF, the skin effect is negligible in most underground materials. Simple magnetic dipole model can be still used in most common underground scenarios, since we are still operating on the near field region [18], [19]. The real-world experiment confirms beyond any doubt the validity of the model in the man-made cave we considered.

B. Triaxial Magnetic Channel

The magnetic source (referred to as a transmitter, TX for parity with conventional RF positioning) is equipped with three mutually perpendicular *triaxial* coils which can be individually energized with a low frequency modulated current to generate a quasi-static magnetic field [11]. A triaxial sensor (referred to as a receiver, RX) can detect the vector field created by the TX. As the position and orientation of the RX is changed relative to the TX, the received signals will also change in terms of amplitude and phase. The *magnetic channel matrix* is a 3×3 matrix that relates the three TX coils to the three RX coils (like in MIMO communications). The magnetic channel matrix contains the RX's 3-D position and orientation information, and its characterization is therefore fundamental for localization.

Consider a magnetic TX located at the origin of a local coordinate frame. Let $\mathbf{r}$ be the RX 3-D position vector, and $\mathbf{\Omega}_{\text{t}} \in SO(3)$ an orthogonal matrix that expresses the orientation of the RX frame in the TX frame. Our goal is to provide a model which can be used to estimate the RX 3-D position and orientation, using the received triaxial magnetic signals only. In this paper, we adopt a space-time magnetic vector modulation [24], where each TX axis generates a BPSK encoded signal sequentially. Consider a $3\times S$ matrix $\mathbf{P}_{\text{tx}}$ whose rows contain the S symbols that are transmitted subsequently over each of the three coils. Let $\mathbf{P}_{\text{rx}} = \mathbf{S}\mathbf{P}_{\text{tx}} + \mathbf{V}$ be the corresponding sequence received at the RX triaxial coil, where $\mathbf{S}$ is the 3×3 magnetic channel matrix, and $\mathbf{V}$ is the zero-mean white Gaussian noise. The entries $s_{j,i}$ of $\mathbf{S}$ express the energy transferred from the ith TX coil to the jth RX coil, as well as the relative phases of the currents in the triaxial coils. At extremely low frequencies (here, a 2.5 KHz carrier is used), the channel matrix can be predicted in free-space using the magnetic dipole equations [15], [16], and may be expressed

in terms of RX position and orientation as follows (the proof is provided in [11])

$$\mathbf{S} = c\boldsymbol{\Omega}_{\mathrm{t}}^{T}\left[\frac{3\mathbf{r}\mathbf{r}^{T}}{r^{2}} - \mathbf{I}_{3}\right]. \tag{1}$$

where c is a range-dependent scaling factor, $r = \|\mathbf{r}\|_2$ is the TX-RX range, $\mathbf{I}_3$ is the 3×3 identity matrix, and $(\cdot)^T$ denotes the matrix transpose. The scaling factor $c \propto r^{-3}$ decays with the cube of the distance, and also incorporates the TX/RX coils and transceiver chain specific parameters (number of turns in the coils, their cross-sectional areas, core magnetic permeability, driving current, amplifier gains and operation frequency), and can easily be determined by calibration from a single measurement taken at a known distance [11]. Note that the channel matrix $\mathbf{S}$ in Eq. (1) depends on the position vector $\mathbf{r}$ and the orientation $\boldsymbol{\Omega}_{\mathrm{t}}$ we are interested in, and can be estimated at the RX using the training sequence $\mathbf{P}_{\mathrm{tx}}$, as is typically done in wireless communications (e.g. by least-squares estimation [11]).

C. 3-D Position and Orientation Estimation – Single TX Case

In this section, we overview the principles of magneto-inductive localization for a single TX-RX pair. We extend this in Sec. III to the case of multiple TX-RX pairs. Both the position $\mathbf{r}$ and the orientation $\boldsymbol{\Omega}_{\mathrm{t}}$ of the RX in 3-D can be estimated solely based on the received triaxial magnetic channel matrix $\mathbf{S}$ in Eq. (1). Using linear algebra, it is possible to find either the position or the orientation independently i.e. the channel matrix can be reformulated to be rotationally invariant or translationally invariant respectively. We first describe how to find the position of the RX, followed by orientation.

1) RX 3-D Position Estimation : First, we determine the range from the overall received power at the three RX axes, which corresponds to the squared Frobenius norm of $\mathbf{S}$. We define the overall RSSI (Received Signal Strength Indicator) measured in dB as

$$\rho \triangleq 20\log_{10}\|\mathbf{S}\|_{\mathrm{F}}. \tag{2}$$

Since $\|\mathbf{S}\|_{\mathrm{F}} \propto r^{-3}$, in the near field, the corresponding RSSI decays at a rate of 60 dB/decade [25], and can be used for range estimation [11]. The law describing the RSSI vs. distance in free-space is

$$\rho = \rho_0 - 60\log_{10}(r/r_0) + \eta, \tag{3}$$

where ρ_0 is the RSSI measured at some reference distance r_0 (determined by calibration) and r is the distance between TX and RX. The uncertainties that contribute to the RSSI measurement, corresponding to the residuals in Figure 1(a), are well-approximated by a zero-mean Gaussian distribution $\eta \sim \mathcal{N}(\eta; 0, \sigma^2)$. This assumption is quite common in wireless communications, and is also supported by our experiments. Thus, the maximum likelihood estimate of the range is

$$\hat{r} = r_0 10^{(\rho_0-\rho)/60}. \tag{4}$$

The magnetic RSSI model and the corresponding ranging errors derived from underground measurements are shown in

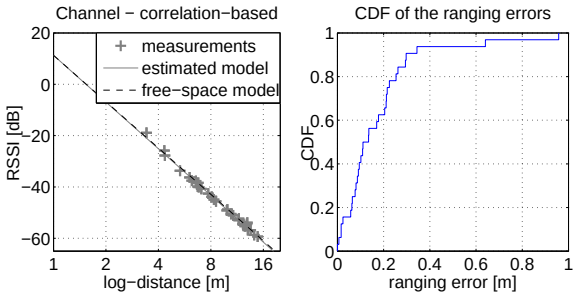

Fig. 1. Through-the-earth magnetic ranging. Path-loss channel model estimated from underground measurements vs. free-space model (left). The CDF of the corresponding ranging estimation errors (right).

Fig. 1. The left subplot in Fig. 1 shows the measured magnetic RSSI as a function of log-distance, as well as the estimated underground channel model which is very close to the free-space channel model. Since there is no multipath and fading, the variance of the residual error is extremely low, unlike RF RSSI. Moreover, the steep slope of the linear model allows for very accurate ranging, and detect tiny displacements, as demonstrated in [11]. The right subplot in Fig. 1 shows the CDF of the range estimation errors using the magnetic RSSI, as in Eq. (4). Using our through-the-ground measurements, we concluded that the tested underground behaves almost like free-space. We were able to achieve a ranging error less than 30 cm for 90% of the measurements corresponding to distances up to 15 meters. Having the estimated range $\hat{r}$, we only need to determine the direction of the position vector in 3-D, which from now will be called *bearing versor*. The algebraic solution proposed in [11] exploits the rank-one term $\mathbf{r}\mathbf{r}^T/r^2$ in Eq. (1). First, the orientation is removed by defining the so-called channel Gram matrix $\mathbf{C} \triangleq \mathbf{S}^T\mathbf{S}$, and then the RX bearing versor is estimated as its maximal eigenvector $\mathbf{u}_{\max}$. Therefore, the estimated RX position vector expressed in the TX frame can be written as

$$\hat{\mathbf{r}} = \hat{r}\hat{\mathbf{u}}_{\max} \tag{5}$$

where $\hat{\mathbf{u}}_{\max}$ is the maximal eigenvector of the estimated Gram matrix. Due to the symmetry of the magnetic field, the RX 3-D position $\hat{\mathbf{r}}$ can be estimated up to a hemispherical ambiguity, i.e., the solution is either $\hat{\mathbf{r}}$, or $-\hat{\mathbf{r}}$. In the single TX case, the ambiguity may be removed by knowing a minimum amount of information such as "RX is above/below TX" (or on a certain side of an arbitrary plane passing through TX).. By using a second TX, no ambiguities occur.

2) RX Orientation Estimation : The RX orientation matrix $\boldsymbol{\Omega}_{\mathrm{t}}$ can be estimated by combining Eqs. (1) and (5)

$$\mathbf{S} = c\boldsymbol{\Omega}_{\mathrm{t}}^{T}\underbrace{\left[3\mathbf{u}_{\max}\mathbf{u}_{\max}^{T} - \mathbf{I}_{3}\right]}_{\mathbf{P}}, \tag{6}$$

where $\mathbf{P} \triangleq 3\mathbf{u}_{\max}\mathbf{u}_{\max}^{T} - \mathbf{I}_3$ is always an invertible matrix (its eigenvalues are $\{2, -1, -1\}$). The orthogonal Procrustes problem in Eq. (6) can be solved for orthogonal $\boldsymbol{\Omega}_{\mathrm{t}}$ by polar decomposition. The polar decomposition of $c\mathbf{P}\mathbf{S}^T = \mathbf{U}\mathbf{H}$ is a product of an orthogonal matrix $\mathbf{U}$ and a positive semi-definite symmetric matrix $\mathbf{H}$. The nearest matrix satisfying

the equality (6) under Frobenius norm is the orthogonal polar factor of $\mathbf{P}\mathbf{S}^T, \forall c > 0$ (for details, see [26]). Therefore, the matrix describing the orientation of the RX frame in the TX frame is

$$\hat{\mathbf{\Omega}}_{\mathrm{t}} = s\,\mathrm{pf}\{\hat{\mathbf{P}}\hat{\mathbf{S}}^T\}, \tag{7}$$

where $\hat{\mathbf{P}} = 3\hat{\mathbf{u}}_{\max}\hat{\mathbf{u}}_{\max}^T - \mathbf{I}_3$ and $\hat{\mathbf{S}}$ is the estimated channel matrix. For a full-rank matrix $\mathbf{A}$, the polar factor can be calculated as $\mathrm{pf}\{\mathbf{A}\} \triangleq \mathbf{A}(\mathbf{A}^T\mathbf{A})^{-1/2}$. The multiplication by $s \triangleq \mathrm{sign}[\det(\mathrm{pf}\{\hat{\mathbf{P}}\hat{\mathbf{S}}^T\})]$ ensures that $\hat{\mathbf{\Omega}}_{\mathrm{t}}$ is a proper rotation.

III. 3-D Position and Orientation Estimation by Fusing Information from Multiple Transmitters

In Sec. II-C, we showed how the RX 3-D position and orientation can be determined for a single TX-RX pair. In this section, we show how information from multiple transmitters can be fused by a single RX for improved estimation. Let us assume that there are N magneto-inductive infrastructure TXs and one RX carried by the user. Again, we consider position and orientation estimation independently.

A. 3-D position fusion

We express the 3-D position of the RX w.r.t TX in terms of range and bearing versor (a unit vector pointing from a TX in direction of RX).

1) Range likelihood: From Eq. (3), it follows that the likelihood of the range corresponding to the nth TX is

$$l_{\mathrm{r}}(r_n) = \mathcal{N}(\rho_n; \tilde{\rho}_n(r_n), \sigma_n^2), \tag{8}$$

where ρ_n is the measured RSSI, and $\tilde{\rho}_n(r_n) = \rho_{0,n} - 60\log_{10}(r_n/r_{0,n})$ is the RSSI predicted by the path-loss model in Eq. (3) for the range r_n. For the sake of generality, the RSSI model intercept point $\rho_{0,n}$ and variance σ_n^2 may be different for each transmitter n (e.g. depending on the site topography, they may use different transmit powers).

Let $\mathbf{p}$ and $\mathbf{t}_n$ denote the position vectors in the world frame corresponding to the RX and the nth TX, respectively. Then, the range can be expressed as $r_n = \|\mathbf{p} - \mathbf{t}_n\|$. In lack of other information concerning correlation among adjacent location estimation errors, we assume that the RSSI uncertainties are mutually independent for all N transmitters. Therefore, the joint log-likelihood function including the corresponding ranges is

$$L_{\mathrm{r}}(\mathbf{p}) = \mathrm{c}_1 - \sum_{n=1}^{N} \frac{1}{2\sigma_n^2}\left(\rho_n - \rho_{0,n} + 60\log_{10}\frac{\|\mathbf{p}-\mathbf{t}_n\|}{r_0}\right)^2, \tag{9}$$

where c_1 is a constant that does not depend on $\mathbf{p}$.

Fig. 2 illustrates the range joint likelihood function for 2 transmitters. The two spheres have radii equal to the most likely range, and the likelihood function is maximized at their intersection. True RX position is shown by the black dot.

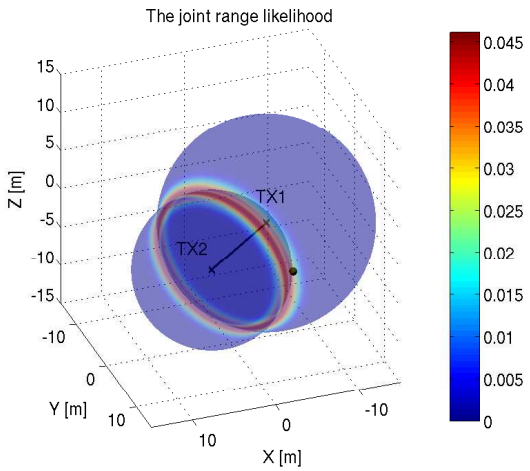

Fig. 2. Illustration of the range joint likelihood function for 2 TXs. The two spheres have radius equal to the estimated range, and the likelihood function is maximized at their intersection. True RX position is shown by the black dot.

2) Bearing Angle Likelihood: Unlike conventional range-based multilateration, we are able to estimate angles between transceivers in 3-D. In order to deal with angular uncertainties, we need probability density functions defined in a proper parameter space, which is the 2-sphere. We model the bearing versor angular error using von Mises-Fisher distribution, which is defined for the random 3-dimensional unit vector $\mathbf{x} \in \mathbb{R}^3$ as follows:

$$p(\mathbf{x}; \boldsymbol{\mu}, \kappa) = \frac{\kappa}{4\pi \sinh \kappa} \exp(\kappa \boldsymbol{\mu}^T \mathbf{x}), \tag{10}$$

where $\boldsymbol{\mu}$ is a unit vector pointing in the mean direction, and κ is the concentration parameter. The reason for choosing the von Mises-Fisher distribution is that it is perhaps the simplest distribution defined on a unit sphere that describes measures such as central tendency and variance similarly to the Gaussian distribution on Euclidean spaces. In order to deal with the hemispherical ambiguity in position estimation which magneto-inductive positioning is subject to due to the field symmetry, we use a balanced mixture of two Fisher distributions [27] whose means correspond to the estimated position versor of the nth TX $\hat{\mathbf{u}}_n = \hat{\mathbf{r}}_n/r$ in Eq. (5), and its antipodal point $-\hat{\mathbf{u}}_n$, respectively. To the best of our knowledge, mixture of such distributions has been used in the context of antenna arrays [27], but not for magneto-inductive positioning. The corresponding bimodal bearing likelihood for the nth TX is $l_{\angle}(\mathbf{r}) = [p(\mathbf{r}; \hat{\mathbf{u}}_n, \kappa_n) + p(\mathbf{r}; -\hat{\mathbf{u}}_n, \kappa_n)]/2$, i.e.,

$$l_{\angle}(\mathbf{r}) = \frac{\kappa_n}{4\pi \sinh \kappa_n} \cosh(\kappa_n \hat{\mathbf{u}}_n^T \mathbf{r}). \tag{11}$$

For N transmitters, the joint log-likelihood function that includes the estimated bearing versors $\hat{\mathbf{u}}_n = (\hat{\mathbf{p}} - \mathbf{t}_n)/\|\hat{\mathbf{p}} - \mathbf{t}_n\|$ is

$$L_{\angle}(\mathbf{p}) = \mathrm{c}_2 + \sum_{n=1}^{N} \ln\ \cosh\left[\kappa_n \frac{(\mathbf{p}-\mathbf{t}_n)^T}{\|\mathbf{p}-\mathbf{t}_n\|}\frac{(\hat{\mathbf{p}}-\mathbf{t}_n)}{\|\hat{\mathbf{p}}-\mathbf{t}_n\|}\right], \tag{12}$$

where c_2 is a constant that does not depend on $\mathbf{p}$.

When fusing 3-D position estimates from multiple transmitters, it is crucial to find suitable weights for the angular errors. In order to set the concentration parameter κ_n which characterizes the spread of von Mises-Fisher p.d.f., we exploit the eigenstructure of the Gram channel matrix $\mathbf{C}$ as in [11]. In Eq. (1), we may notice that the eigenvalues of $\mathbf{C} = \mathbf{S}^T\mathbf{S}$ are $\{4c^2,\ c^2,\ c^2\}$ (the maximum eigenvalue is four times larger than the remaining two, as expected from the dipole equation) [28]. In order to eliminate the range-dependent scaling factor c, we divide by the average of the eigenvalues (which is $2c^2$), and we obtain the following scaled eigenvalue vector

$$\boldsymbol{\lambda} = [2,\ \frac{1}{2},\ \frac{1}{2}]^T. \tag{13}$$

In an undistorted environment, the vector $\boldsymbol{\lambda}$ remains constant *regardless* of the locations and orientations of TX and RX. Therefore, any deviations from this may be caused the presence of distortions in the environment, as shown in [11]. Distortions are caused by large amounts of ferrous materials, typically steel mesh used in the cave reinforcement or heavy machinery. In order to quantify the change in the eigenvalues spread, we use the criterion proposed in [11] that penalizes the departure of the estimated scaled eigenvalue vector $\hat{\boldsymbol{\lambda}}_n$ from the theoretical free-space value $\boldsymbol{\lambda}$, i.e.,

$$\mathcal{J}(\hat{\boldsymbol{\lambda}}_n) = (\|\hat{\boldsymbol{\lambda}}_n - \boldsymbol{\lambda}\|_2)/\|\boldsymbol{\lambda}\|_2, \tag{14}$$

where $\hat{\boldsymbol{\lambda}}_n$ corresponds to the eigenvalues of the nth TX's estimated Gram matrix $\hat{\mathbf{C}}_n = \hat{\mathbf{S}}_n^T\hat{\mathbf{S}}_n$ sorted in descending order, and divided by their average. Large values of the criterion $\mathcal{J}(\hat{\boldsymbol{\lambda}}_n)$ criterion show that the channel eigenstructure deviates from the triaxial dipoles, and therefore, the angle estimation will be poor, as also demonstrated in [11].

Fig. 3(a) shows the value of the criterion vs. angular estimation errors obtained from real-world measurements in three different scenarios: outdoor undistorted environment (with no ferrous materials), indoors (reinforced concrete and massive building structures), and cave scenario (unknown distortion sources). We may notice that in the undistorted outdoor environment [green "+" markers in Fig. 3(a)], both the angular errors and the values of the criterion $\mathcal{J}$ are small. Indoors, large angular errors tend to be associated with large values of $\mathcal{J}$ [red "$\circ$" markers in Fig. 3(a)]. Many of the very large angular errors occur when the channel matrix is singular [shown by magenta "$\times$" markers in Fig. 3(a)], and can be detected and discarded from the angle estimation. Unlike outdoors and indoors, it was impossible to tell in advance whether the cave measurement data are distorted or not. The cave measurement data [shown by the blue star markers in Fig. 3(a)] seem to be more similar to the undistorted outdoor data. This is the case of many underground environments, as the extremely low frequency magnetic field penetrates soil, rock and concrete practically the same as free-space [17], [24], [29], [30].

Overall, the relationship between the value of the criterion $\mathcal{J}$ and the angular error is not obvious in Fig. 3(a), and therefore, we attempt to predict the angular error from $\mathcal{J}$ in a probabilistic manner. We model the 2-D histogram of the data in Fig. 3(a) as a p.d.f parametrized by 4 parameters,

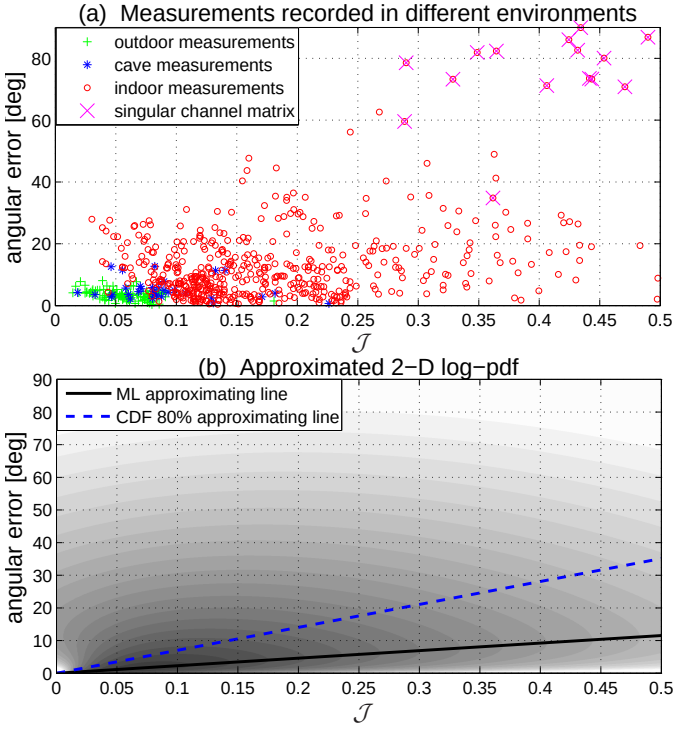

Fig. 3. (a) Angular estimation errors vs. eigenvalue criterion $\mathcal{J}$ for measurements collected in 3 different environments. The largest angular errors occur when the channel matrix is singular. (b) 2-D log-pdf fit. The most likely angular error for a given value of $\mathcal{J}$ corresponds to the maximum value of the density along the vertical dimension. These maxima lie approximately along a straight line (black line). The 80% confidence bound for the angular error is shown by the continuous blue line.

and estimate the most likely value of the angular error given a value of $\mathcal{J}$. Due to the shape of the histogram, polar coordinates seem more appropriate. In order to obtain a smooth 2-D histogram a very large number of points would be necessary. Therefore, we approximate the histogram by using two independent log-normal random variables for radius and angle, respectively (4 parameters in total). The resulting 2-D log-p.d.f. approximation is shown in Fig. 3(b). For a given value of $\mathcal{J}$, the most likely value of the angular error corresponds to the maximum value of the density along the vertical dimension. The maxima lie approximately along a straight line (black line in Fig. 3(b). These estimates are rather optimistic, i.e. there are many cases when the error is underestimated, and this may give too much confidence on poor estimates. A more reliable approach is to ensure that the predicted angular error is less than the actual error with a certain probability. The 80% confidence bound is shown by the blue dotted line in Fig. 3, for a given value of $\mathcal{J}$. Therefore, the angular error confidence bound is predicted as

$$\hat{e}_{\%} = m\mathcal{J}(\hat{\boldsymbol{\lambda}}_n), \tag{15}$$

where $m = 1.2$ is the slope of the 80% confidence line when the angle is measured in radians (in Fig. 3). Given this bound, we need to find the concentration parameter κ_n of the von Mises-Fisher distribution such that the semi-vertical angle of the confidence cone comprises 80% of the samples. The confidence cone is illustrated in Fig. 4(a). We ran Monte

Carlo simulations to find the value of κ_n given a confidence cone semi-vertical angle value (see Fig. 4(b)). Considering that κ_n behaves like the inverse of the variance, we have found that the concentration parameter for the nth TX can be very well approximated as

$$\hat{\kappa}_n = \frac{3.25}{\hat{e}^2_{\%}}. \tag{16}$$

where the predicted angular error confidence bound is given in Eq. (15), and this corresponds to the semi-vertical angle of the confidence cone. This very simple approximation matches very well the Monte Carlo simulation, as shown in Fig. 4(b).

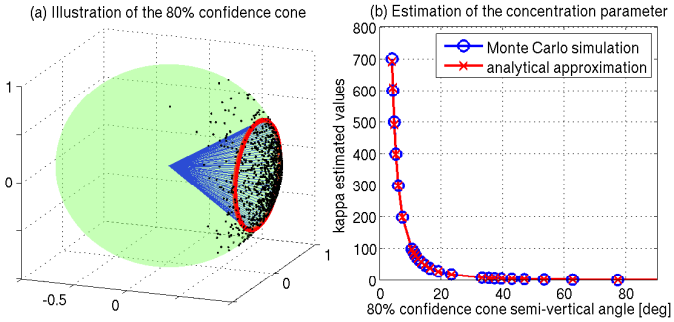

Fig. 4. Estimation of the concentration parameter κ_n. (a) The 80% confidence cone (blue) is illustrated on the unit sphere for random von Mises-Fisher samples (black dots) and $\kappa_n = 10$. (b) The estimated κ_n using Monte Carlo simulations (blue curve with circle markers) and the corresponding analytical approximation (red curve with cross markers) for a given value of the confidence cone semi-vertical angle.

Fig. 5 illustrates the bimodal angular likelihoods corresponding to two transmitters. The 3-D hemispherical ambiguity can be completely removed using at least two TXs.

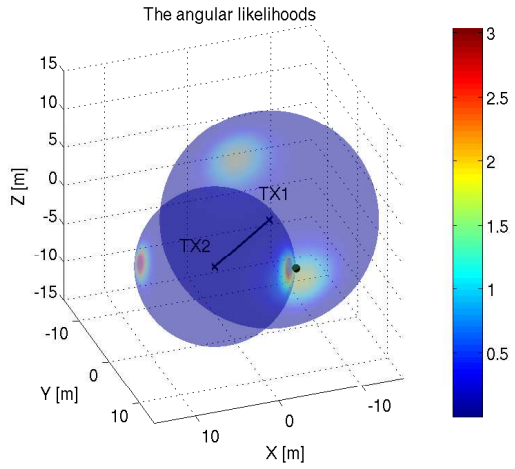

Fig. 5. Illustration of the independent angular likelihood function for 2 TXs. Each likelihood is maximized at two antipodal points. True RX position is shown by the black dot.

3) Joint Log-likelihood Maximization: Our goal is to maximize the joint log-likelihood corresponding to the N TXs that includes range and 3-D bearing information

$$L(\mathbf{p}) = L_{\mathrm{r}}(\mathbf{r}) + L_{\angle}(\mathbf{r}), \tag{17}$$

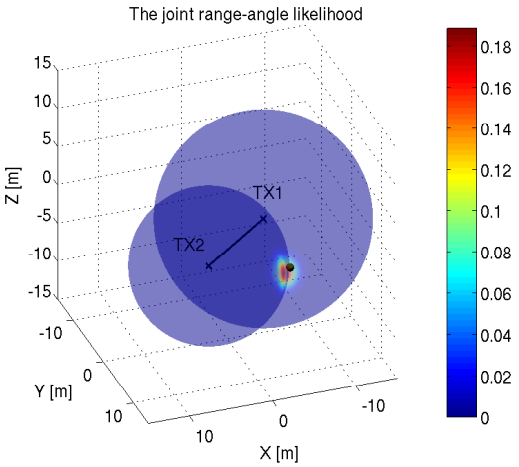

Fig. 6. Illustration of the joint range-bearing likelihood function for two transmitters TX1 and TX2. The two spheres correspond to the most likely ranges. The joint likelihood is maximized close to the true RX position (shown by the black dot).

and this is achieved by using a steepest ascent algorithm. Fig. 6 shows that the joint range and bearing likelihood function has a well-defined maxima in the vicinity of the true position. The ML position estimate at iteration k is

$$\hat{\mathbf{p}}^{(k)} = \hat{\mathbf{p}}^{(k-1)} + \gamma \Big[\frac{\mathrm{d}L}{\mathrm{d}\mathbf{p}}\Big]_{\mathbf{p}=\hat{\mathbf{p}}^{(k-1)}}, \tag{18}$$

where γ is the step size, and $[\mathrm{d}L/\mathrm{d}\mathbf{p}]_{\mathbf{p}=\hat{\mathbf{p}}^{(k-1)}}$ is the gradient vector of the joint likelihood function evaluated at $\hat{\mathbf{p}}^{(k-1)}$. The gradient expression is given by

$$\begin{aligned}\frac{\mathrm{d}L}{\mathrm{d}\mathbf{p}} &= -\frac{60}{\ln\ 10}\sum_{n=1}^{N}\frac{(\rho_n - \rho_{0,n} + 60\log_{10}\|\mathbf{p}-\mathbf{t}_n\|)}{\sigma_n^2\|\mathbf{p}-\mathbf{t}_n\|^2}(\mathbf{p}-\mathbf{t}_n) \\ &+ \sum_{n=1}^{N}\tanh\Big[\kappa_n\frac{(\mathbf{p}-\mathbf{t}_n)^T}{\|\mathbf{p}-\mathbf{t}_n\|}\frac{(\hat{\mathbf{p}}-\mathbf{t}_n)}{\|\hat{\mathbf{p}}-\mathbf{t}_n\|}\Big]\times \\ &\times\kappa_n\Big[\mathbf{I}_3 - \frac{(\mathbf{p}-\mathbf{t}_n)(\mathbf{p}-\mathbf{t}_n)^T}{\|\mathbf{p}-\mathbf{t}_n\|^2}\Big]\frac{(\hat{\mathbf{p}}-\mathbf{t}_n)}{\|\hat{\mathbf{p}}-\mathbf{t}_n\|}\Big].\end{aligned} \tag{19}$$

B. 3-D Orientation fusion

In order to fuse the orientation estimates from N different transmitters, we need to combine multiple rotation matrices. The problem of means and averaging in the group of $n \times n$ rotations $SO(n)$ has been extensively studied in applied mathematics and robotics (see [31], [32]). In this paper, we use the projected barycentric mean method, where the average of the estimated rotations is projected onto $SO(3)$ using polar decomposition [31]. The orientation matrix after the fusion is obtained as the orthogonal polar factor of the average of the independently estimated rotations $\hat{\mathbf{\Omega}}_n$:

$$\hat{\mathbf{\Omega}} = \mathrm{pf}\Big\{\sum_{n=1}^{N}\hat{\mathbf{\Omega}}_n\Big\}. \tag{20}$$

IV. System Architecture and Operation

The proposed system consists of several magnetic TXs (which constitute the infrastructure), and RXs (which are the user devices). By *"single anchor"*, we mean the only TX in the entire network whose position and orientation are known, either in global coordinates, or it is used as a local origin for the whole network. The remaining TXs whose positions and orientations are unknown, and need to be estimated, are called *secondary TXs*. In this section, we describe the two operation modes of the proposed system: *1) network deployment and discovery mode* and *2) user localization mode*. In the network deployment and discovery mode, the goal is to automatically determine all the positions and orientations of the secondary TXs, using received magnetic signals from those secondary TXs, as well as from the single anchor node, or from other secondary TXs whose positions and orientations have been estimated. In this mode, RX localization is a secondary goal, i.e., it is just required to aid the discovery of the spatial topology of the network. Once all TXs have been localized, they may act as new anchor nodes. The user localization mode is the normal operation mode with the goal of determining the RX position and orientation. This paper addresses both operation modes of the system.

A. Network Deployment and Discovery Mode

In the network deployment and discovery mode, the infrastructure is installed in the area of interest. Note that the infrastructure can be incrementally deployed, for example, as a cave is explored, more TXs can be installed to maintain coverage. The goal of this mode is to determine the location and orientation of all TXs in the network. The rapid network deployment mode consists of three phases, which are illustrated in Fig. 7 and explained as follows:

Phase I: The system starts with a single anchor node, a TX whose position and orientation are known with respect to the global frame, e.g. at the tunnel entrance. If a global coordinate system is not needed, this can simply be assigned as the origin of a local system of coordinates for relative positioning. Using signals received from the TX, a RX finds its own 3-D position and orientation in the anchor's frame.

Phase II: Several RX positions, which from now will be referred to as "RX test locations" are used to estimate the 3-D positions and orientations of all the other secondary TXs in range, as the RX moves away from the single anchor.

Phase III: All TXs in range act as new anchors. The RX now refines its position using the MI signals from all TXs and ML estimation. However, the positions of either the secondary anchors or the RX could be inaccurate, as they are based on only a few measurements. A joint iterative TX/RX position and orientation refinement procedure is used to improve the estimates of the secondary anchors. As more measurements are taken, the spatial network topology reaches a steady state. This concludes the network discovery mode phase and the MI network is now ready to achieve full 3-D RX position and orientation estimation.

Note that all computation is performed at the RX - there is no need for a bidirectional communication link between TXs and RXs. As the system is RX-centric, the number of RXs that the system supports is practically unlimited. There is no need for the TXs to know the RX location. Each RX can operate independently to determine its own position and orientation based on the beacons continuously sent by the TXs. Multiple RXs could of course share position estimates to increase convergence speed, but in this paper for simplicity we consider the case of a single RX.

The complete algorithm behind the network deployment and discovery strategy is presented in detail in Section V.

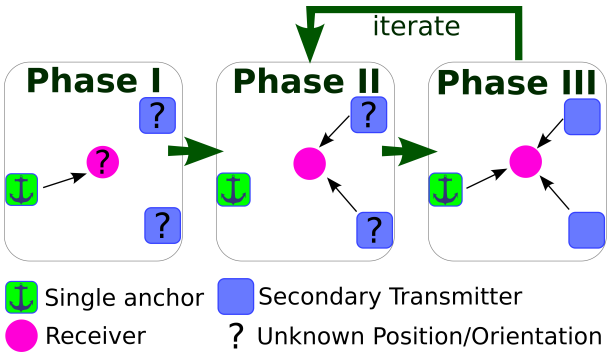

Fig. 7. *Single anchor* localization network deployment. **Phase I:** RX finds its own 3-D position and orientation using the MI signal from the anchor node. **Phase II:** Several RX positions, which from now will be referred to as "RX test locations" are used to estimate the 3-D positions and orientations of all the other TXs in range. **Phase III:** All TXs in range act as new anchors. TX/RX positions and orientations are then refined iteratively.

B. User Localization Mode

This is the normal operation mode of the magnetic network, and its goal is to determine the RX position and orientation using the deployed infrastructure. In this phase, it is assumed that the locations of all anchors are known. Using signals from one or more TXs in range, a RX can compute its 3-D position and orientation.

V. Network Deployment and Discovery Algorithm

In this section, we describe in detail the algorithm that enables rapid network deployment. First, we explain the single anchor concept used for estimating the initial network spatial topology. Then, we provide the iterative refinement procedure that fine-tunes the initial topology in order to improve the overall localization accuracy.

A. Single Anchor System Deployment

In this section, we describe our core contribution, a technique for determining the positions of all unsurveyed TXs relative to the single anchor. The key novelty of our system is that it only requires *a single* TX whose position and orientation are known accurately. This node acts as a single anchor node for the entire network and can be placed, for example, at the entrance of the cave, where it is easy to get global coordinates, e.g. using satellite navigation solutions. Using this anchor node, the positions and orientations of the secondary TXs

can be determined with high accuracy, provided that there are locations where the RX carried by the user receives signal both from the anchor and from those TXs whose positions and orientations need to be estimated. Once the positions and orientations of those TXs have been determined, they can further act as new anchors, until the positions and orientations of all TXs in the network have been identified.

The "single anchor" concept simply cannot be used with the conventional range-based localization systems. In order to achieve 3-D localization, such systems require at least four anchor nodes whose positions are known with high accuracy. In underground environments with tortuous tunnels, this is extremely difficult to ensure. Moreover, accurate 3-D positioning requires that these anchors exhibit a very good geometric configuration almost everywhere (geometric dilution of precision), which is very impractical. For example, if all four nodes lie on a plane, or on a line, as often happens along tunnels, the 3-D position becomes ambiguous, or exhibits very high variance in certain directions. This is not the case in our proposed system, since with a single TX, it is possible to determine both position and orientation of a RX in 3-D. Those are subject to hemispherical ambiguity which can easily be removed based on a very rough knowledge of the map, for example just knowing which half-side of the TX to choose). Note that the proposed single anchor approach differs from the robot relative pose estimation [33] in several aspects: i) instead of using multiple cooperating agents, our RX is moved at different test locations; ii) our approach is for 3-D positioning, not for 2-D; iii) unlike [33], we require a single anchor (landmark) instead of two (or three in 3-D) in order to unambiguously solve for positions and orientations of *all* network nodes; iv) no inertial sensors are required.

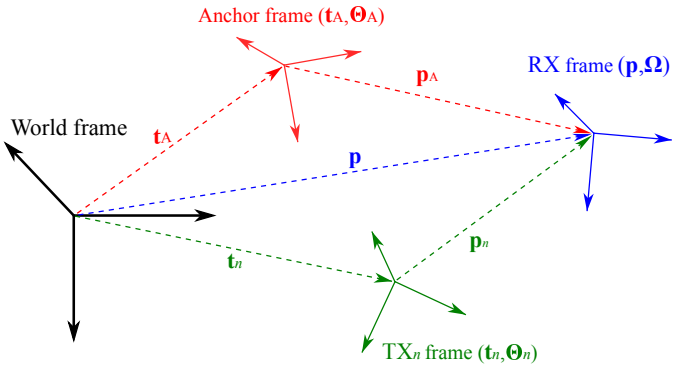

Fig. 8. Single anchor localization. First, the RX position $\mathbf{p}$ and orientation $\mathbf{\Omega}$ in the world frame are estimated using the anchor TX_A. Using these estimates, the position $\mathbf{t}_n$ and orientation $\mathbf{\Theta}_n$ of TX_n are determined using its triaxial signal received at RX.

The single anchor concept is illustrated in Fig. 8. We assume that there is one anchor node TX_A whose position $\mathbf{t}_\text{A}$ and orientation $\mathbf{\Theta}_\text{A}$ in the world frame are known. The anchor TX_A frame is shown in red color. The world coordinate frame is shown in black color. The nth TX position $\mathbf{t}_n$ and orientation $\mathbf{\Theta}_n$ (shown in green color in Fig. 8) are unknown for all N secondary TXs. The network deployment and discovery mode consists of the three phases introduced in Section IV.

Phase I: RX position $\mathbf{p}$ and orientation $\mathbf{\Omega}$ in the world frame (shown in blue color in Fig. 8) are determined using the anchor node TX_A, as described in Section II-C1.

Phase II: The nth TX position $\mathbf{t}_n$ and orientation $\mathbf{\Theta}_n$ in the world frame are determined from the estimated relative position and orientation w.r.t. to RX. The procedure will be described in Sections V-A2 and V-A1, respectively.

Phase III: The TX and RX positions and orientations are re-estimated iteratively, as detailed in Section V-B.

Obviously, as we depart from the single anchor (origin), the global accuracy of the map degrades. Possible loops in the network spatial topology may be exploited to spread the error across the network, and prevent the error accumulation in a SLAM-like fashion [34]. However, if no loops are available, despite the degradation of global accuracy, the estimated spatial topology is locally accurate, similarly to distributed multi-dimensional scaling [35]. The secondary anchors may be used as landmarks to provide locally accurate relative position and orientation estimation.

1) TX Position Estimation using Single Anchor: The procedure is as follows. Let $\mathbf{r}_\text{A}$ be the RX position vector expressed in the local frame of the anchor node TX_A, whose position vector $\mathbf{t}_\text{A}$ and orientation $\mathbf{\Theta}_\text{A}$ in the world frame are known. The RX position in the world frame using the anchor node may be written as:

$$\mathbf{p} = \mathbf{t}_\text{A} + \mathbf{\Theta}_\text{A}\mathbf{r}_\text{A} \tag{21}$$

Similarly, using the nth TX, the RX position the may be written as:

$$\mathbf{p} = \mathbf{t}_n + \mathbf{\Theta}_n\mathbf{r}_n, \tag{22}$$

where the nth TX position $\mathbf{t}_n$ is unknown, and needs to be determined. From Eqs. (21) and (22), and using the estimated values instead of the true ones, we can write:

$$\hat{\mathbf{t}}_n = \mathbf{t}_\text{A} + \mathbf{\Theta}_\text{A}\hat{\mathbf{r}}_\text{A} - \hat{\mathbf{\Theta}}_n\hat{\mathbf{r}}_n, \tag{23}$$

where $\hat{\mathbf{r}}_\text{A}$ and $\hat{\mathbf{r}}_n$ are the RX positions estimated in the local frames of the anchor TX_A, and in the frame of the nth TX, respectively, from the corresponding magnetic signals. The matrix $\hat{\mathbf{\Theta}}_n$ is the estimated orientation of the nth TX in the world frame, and the corresponding estimation problem is addressed in Section V-A2. Measurements collected at two different locations from both the anchor TX and the nth TX whose position and orientation are unknown are sufficient to unambiguously estimate the nth TX position. Assuming that M measurements collected at different RX positions are available, the nth TX position estimation can be improved by averaging over all estimated positions:

$$\hat{\mathbf{t}}_n^M = \mathbf{t}_\text{A} + \mathbf{\Theta}_\text{A}\bar{\hat{\mathbf{r}}}_\text{A} - \hat{\mathbf{\Theta}}_n^M\bar{\hat{\mathbf{r}}}_n, \tag{24}$$

$\bar{\hat{\mathbf{r}}}_\text{A} = (1/M)\sum_{m=1}^{M}\hat{\mathbf{r}}_{\text{A},m}$, and $\bar{\hat{\mathbf{r}}}_n = (1/M)\sum_{m=1}^{M}\hat{\mathbf{r}}_{n,m}$ are the centers of mass of the mth estimated position vectors $\hat{\mathbf{r}}_{\text{A},m}$ and $\hat{\mathbf{r}}_{n,m}$, respectively, with $m = 1, \ldots, M$.

2) TX Orientation Estimation using Single Anchor: Accurately knowing the TX orientation is crucial for 3-D magnetic positioning, as an orientation error of just 10° causes a 3-D positioning error of about 3.5 meters at 10 meters away from the TX, even if the range is estimated perfectly. We propose an approach for TX orientation estimation, and show experimentally that it is capable to achieve errors of around 5°, in the presence of ranging errors.

Let $\mathbf{\Omega}_\mathrm{A}$ be the RX orientation expressed in the local frame of the anchor node $\mathrm{TX_A}$, which can be estimated from the triaxial magnetic signal received from the anchor using Eq. (7). The RX orientation in the global frame $\mathbf{\Omega}$ can be expressed as:

$$\mathbf{\Omega} = \mathbf{\Theta}_\mathrm{A}\mathbf{\Omega}_\mathrm{A}. \tag{25}$$

A similar equation can be written for the nth TX whose orientation $\mathbf{\Theta}_n$ in the world frame is unknown

$$\mathbf{\Omega} = \mathbf{\Theta}_n\mathbf{\Omega}_n, \tag{26}$$

where $\mathbf{\Omega}_n$ is the RX orientation expressed in the local frame of TX_n, and which can be determined from the corresponding magnetic signal. From Eqs. (25) and (26), the estimated TX_n in the world frame may be written as:

$$\hat{\mathbf{\Theta}}_n = \mathbf{\Theta}_\mathrm{A}\hat{\mathbf{\Omega}}_\mathrm{A}\hat{\mathbf{\Omega}}_n^T, \tag{27}$$

where $\hat{\mathbf{\Omega}}_\mathrm{A}$ and $\hat{\mathbf{\Omega}}_n$ are the estimated local RX orientations in the $\mathrm{TX_A}$ frame and the nth TX frame, respectively. Assuming that M measurements collected at different RX positions are available, the nth TX orientation estimation can be improved. Let $\bar{\hat{\mathbf{\Omega}}}_\mathrm{A} = [\hat{\mathbf{\Omega}}_{\mathrm{A},1}, \ldots, \hat{\mathbf{\Omega}}_{\mathrm{A},M}]$ be a collection of RX orientation estimates $\hat{\mathbf{\Omega}}_{\mathrm{A},m}$ from the anchor TX at each position $m = 1, \ldots, M$. Similarly, let $\bar{\hat{\mathbf{\Omega}}}_n = [\hat{\mathbf{\Omega}}_{n,1}, \ldots, \hat{\mathbf{\Omega}}_{n,M}]$ be a collection of RX orientation estimates $\hat{\mathbf{\Omega}}_{n,m}$ from the nth TX, $m = 1, \ldots, M$. Then, we obtain

$$\mathbf{\Theta}_\mathrm{A}\bar{\hat{\mathbf{\Omega}}}_\mathrm{A} = \mathbf{\Theta}_n\bar{\hat{\mathbf{\Omega}}}_n. \tag{28}$$

Using the fact that $\bar{\hat{\mathbf{\Omega}}}_n\bar{\hat{\mathbf{\Omega}}}_n^T = M\mathbf{I}_3$, we can write:

$$\bar{\hat{\mathbf{\Theta}}}_n = \frac{1}{M}\mathbf{\Theta}_\mathrm{A}\bar{\hat{\mathbf{\Omega}}}_\mathrm{A}\bar{\hat{\mathbf{\Omega}}}_n^T \tag{29}$$

Obviously, in the presence of orientation estimation errors, Eq. (29) does not hold exactly, and the result will not be an orthogonal matrix. The solution is to use the projected mean onto $SO(3)$ using polar decomposition [31]. The nth TX orientation estimated from measurements collected at M positions is the orthogonal polar factor of $\bar{\hat{\mathbf{\Theta}}}_n$

$$\hat{\mathbf{\Theta}}_n^M = \mathrm{pf}\{\bar{\hat{\mathbf{\Theta}}}_n\}. \tag{30}$$

B. Joint Iterative TX/RX Positions and Orientations Refinement Algorithm

The single anchor estimation approach just described in Section V-A can be used to obtain very good initial estimates of the TX positions and orientations. After determining their positions and orientation, these new TXs act as new anchors, and ML can be used to refine the RX position and orientation. Then, the new RX position and orientation can help to refine the TX position and orientation estimates. The procedure can be iterated until a steady-state is reached. The steady state may be evaluated by comparing the changes in positions and orientation from an iteration to the next iteration to a certain threshold.

The stopping criteria for the position refinement quantifies the average variation of subsequent TX positions estimates $\hat{\mathbf{t}}_n$ for all N TXs, and RX position estimates $\hat{\mathbf{p}}_m$, for all M RX positions.

$$\frac{1}{N}\sum_{n=1}^{N}\|\hat{\mathbf{t}}_n^{(k-1)} - \hat{\mathbf{t}}_n^{(k)}\| + \frac{1}{M}\sum_{m=1}^{M}\|\hat{\mathbf{p}}_m^{(k)} - \hat{\mathbf{p}}_m^{(k-1)}\| \leq \tau_\mathrm{pos}, \tag{31}$$

where τ_pos is a threshold for the average position changes (can be set to e.g. 0.1 meters)

A similar criterion can be used for the orientation refinement taking into account the geodesic distance between subsequent orientation estimates for both for TX and RX. For two arbitrary rotations $\mathbf{W}_1, \mathbf{W}_2 \in SO(3)$, the geodesic distance [31] is defined as

$$d(\mathbf{W}_1, \mathbf{W}_2) \triangleq \frac{1}{\sqrt{2}}\|\mathrm{Log}(\mathbf{W}_1^T\mathbf{W}_2)\|_\mathrm{F}, \tag{32}$$

where $\mathrm{Log}(\cdot)$ denotes the matrix logarithm. The geodesic distance is the natural metric in the group of rotations $SO(3)$, and has an very intuitive meaning. It corresponds to the angle θ (measured in radians) required to rotate the orthogonal frame defined by $\mathbf{W}_1$ around a fixed axis, such that it overlaps with $\mathbf{W}_2$. The geodesic distance equals $|\theta|$, and is independent of direction of the rotation axis vector. This stems from the Euler theorem of rotations, being intimately related to quaternions. The stopping criterion for orientation changes is

$$\frac{1}{N}\sum_{n=1}^{N}d(\hat{\mathbf{\Theta}}_n^{(k-1)}, \hat{\mathbf{\Theta}}_n^{(k)}) + \frac{1}{M}\sum_{m=1}^{M}d(\hat{\mathbf{\Omega}}_m^{(k-1)}, \hat{\mathbf{\Omega}}_m^{(k)}) \leq \tau_\mathrm{orient}, \tag{33}$$

where τ_orient is a threshold for the average orientation changes (can be set to e.g. 1°) If both the overall position and orientation changes from one iteration to the next one are below the corresponding thresholds, the algorithm terminates.

Algorithm 1 summarizes the joint refinement procedure. The entire algorithm runs on the RX side (RX centric). If passing the information back to a supervisor was required, then obviously, it would imply that the fixed infrastructure is capable of receiving and routing the information to a supervisor. Magneto-inductive communication can be used to achieve through-the-earth communication [24]. Steps 4–5 are used to estimate the initial RX and TXs position and orientation that are iteratively refined in steps 3–8, in a manner similar to iterative multi-dimensional scaling [35].

C. Computational Requirements

In this section, we evaluate the computational cost of the proposed algorithm when it operates in the network deployment and discovery mode, as well as in user localization mode.

1) The cost of network deployment and discovery mode: During network deployment and discovery mode, an RX starts from the anchor and subsequently discovers new secondary TXs. Let N be the number of active TXs heard by the

Inputs: True anchor position and orientation: $\mathbf{t}_{\mathrm{A}}, \mathbf{\Theta}_{\mathrm{A}}$, Estimated channel matrices from TX_{A} and all the others TX_n in range, at all positions m: $\hat{\mathbf{S}}_{\mathrm{A},m}$, and $\hat{\mathbf{S}}_{n,m}, \forall n, m$.
Phase I: Estimate the RX 3-D positions $\hat{\mathbf{p}}_m$ and orientation $\hat{\mathbf{\Omega}}_m, \forall m$ in the world frame using $\hat{\mathbf{S}}_{\mathrm{A},m}, \mathbf{t}_{\mathrm{A}}, \mathbf{\Theta}_{\mathrm{A}}$, and Eqs. (5),(21) and (25).
while steady-state has not been reached in Eqs. (31) and (33) **do**
    Estimate RX 3-D position $\hat{\mathbf{r}}_{n,m}$ and orientation $\hat{\mathbf{\Omega}}_{n,m}$ in the local frames of TX_n in range using, $\mathbf{S}_{n,m}, \forall n, m$, and Eqs. (5), (7).
    Phase II: Estimate TX_n 3-D positions $\hat{\mathbf{t}}_n^M$ and orientations $\hat{\mathbf{\Theta}}_n^M$, $\forall n$ using $\bar{\hat{\mathbf{r}}}_{n,m}, \bar{\hat{\mathbf{\Omega}}}_{n,m}$, and Eqs. (24), (30).
    Phase III: Refine the RX 3-D position $\hat{\mathbf{p}}_m$ and orientation $\hat{\mathbf{\Omega}}_m$ in the world frame using ML estimation in Eqs. (18), (20), $\forall m$ positions. Signals from anchor and all TXs whose positions have been determined are used.
    Refine all TX_n positions and orientations using the new ML estimates (translated into the local frames), as described in item 5.
end while
Outputs: Estimated TX_n 3-D positions $\hat{\mathbf{t}}_n$ and orientations $\hat{\mathbf{\Theta}}_n, \forall n$ TXs. Estimated RX 3-D position $\hat{\mathbf{p}}_m$ and orientation $\hat{\mathbf{\Omega}}_m, \forall m$ RX positions

Algorithm 1: Joint Iterative TX/RX Positions and Orientations Refinement

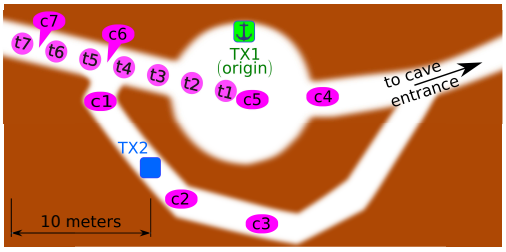

Fig. 9. 2-D schematic layout of cave system (not at scale), showing single anchor (TX1), secondary TX at unknown position (TX2) and test points (t1–t7) where the RX is localized. Note that there are no RF line-of-sight paths between either TX and most RX test locations, or between the two TXs.

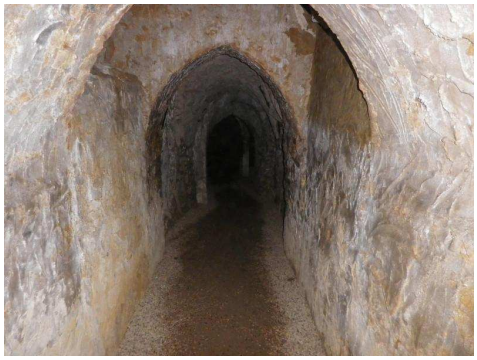

Fig. 10. Cave tunnel.

RX at a given location. In general, $N \leq 5$, in order to decrease the infrastructure cost (minimum is 2, in order to resolve the hemispherical ambiguity). Running the ML algorithm requires a number of inner iterations K_{ML} of the steepest ascent. According to our results, this number is typically less then 100, and can be further decreased by using e.g. a conjugate gradient algorithm. Fusing the position and orientation information from N TXs in range requires an order of complexity of $\mathcal{O}(NK_{\mathrm{ML}})$ at each location. Given a number of RX test locations M for each set of TXs in range, the complexity of estimating all these locations increases to $\mathcal{O}(MNK_{\mathrm{ML}})$. The number of RX test locations ranges between 2 and few tens, depending on the network size. The user moving across the network encounters N_{TX} transmitters. Consequently, a first complete iteration of the joint TX/RX position and orientation estimation procedure requires $\mathcal{O}(N_{\mathrm{TX}}MNK_{\mathrm{ML}})$ computations. The iterative refinement procedure requires few outer iterations K_{ref}. Therefore, the cost of the entire network deployment and discovery procedure involves $\mathcal{O}(K_{\mathrm{ref}}N_{\mathrm{TX}}MNK_{\mathrm{ML}})$ computations. In our simple experiment, $K_{\mathrm{ref}} = 5$ iterations are sufficient to obtain accurate TX/RX position and orientation estimates, but the estimates provided in the first iteration are already accurate enough. The number of iterations might increase with the dimension of the network, but this is not a big issue, as there are no real-time constraints, like in the user localization mode.

2) The cost of user localization mode: The computational cost while operating in user localization mode is of $\mathcal{O}(NK_{\mathrm{ML}})$, and is extremely low, since RX hears $N \in \{2, 3, 4, 5\}$ active TXs, and uses ML to estimate its own position and orientation. The cost is equivalent to few hundreds of matrix operations (of size 3-by-3) for each estimated location, and that is easily achievable by an embedded device. This is the reason why our RX device can operate continuously for more than 12 hours being supplied by a 3.7 V, 1300 mAh Lithium-polymer battery, making it sufficiently small and portable to be used under the ground.

VI. Proof of Concept Experimental Evaluation

In order to validate the proposed proof-of concept, we carried out experiments in the Hellfire Caves (England), which is a network of man-made caverns that mostly consist of humid calcite and mineral quartz. The experiment space measures $15 \times 30 \times 2$ ms^3, as illustrated in Fig. 9. It is well-known that accurately mapping underground caves in 3-D is an extremely difficult and time-consuming task. In order to have a base for evaluation, we surveyed the TX and RX positions using laser-based range and inclination m. Bricks with holes were used as landmarks along the paths, with a thin wire passing through their holes. The distance between consecutive landmarks, as well as the angle between consecutive segments of wire along with the inclination of each segment were carefully measured. In order the reduce the error propagation to subsequent measured landmarks positions, and improve the overall accuracy of the cave map, Graph SLAM algorithm [34] was employed along the semi-circular closed loop in Fig. 9. The loop enclosed the main chamber of circular shape, whose height was several m, unlike the tunnel surrounding it, which was narrow, as shown in Fig. 10. The roof of the main chamber

was supported by a reinforced steel mesh. A small window with steel bars provided view from the semi-circular tunnel to the main chamber. The origin was set closer to the cave entrance, such that its global position can be inferred easily (see Fig. 9). TX1 was placed at the origin and acted as a single anchor, and TX2 was placed in the semi-circular tunnel (their positions and orientations are shown by the green frames). The tunnels were not horizontal, they exhibit a difference in elevation of approximately 2 ms. We performed two different experiments.

The first one, which from now on we will refer to as "linear displacement experiment" corresponds to RX locations `t1` to `t7`, in Fig 9. A measuring tape was laid on the ground and magneto-inductive measurements were collected from TX1 and TX2, every two m along the tape. The surveyed RX 3-D positions and orientations are shown in Fig. 12(a) by the magenta dots and frames, respectively (points `t1` to `t7` in magenta color). The subsequent relative RX orientations were with the x-axis parallel to the tape, pointing in the direction opposite to the center of the main chamber, and the z-axis pointing downwards.

The second experiment which from now on we will refer to as "main chamber experiment" took place in and around the main chamber, whose footprint is approximately circular with average diameter of about 10 m (See Fig. 9). The surveyed RX 3-D positions are shown in Fig. 13(a) by the magenta dots, and the corresponding indices `c1` to `c7`. The true RX orientations were with the x-axis pointing approximately along the path, and the z-axis pointing downwards. TX1 and TX2 were kept at the same positions, and have the same orientations as in the linear displacement experiment.

We used our own hardware to produce and receive modulated magnetic signals. The two TXs and the RX are shown in Fig. 11. TXs are equipped with square triaxial coils (30 cm side, 80 turns, wound on a cubic wooden frame), and the magnetic moment of each coil is about 5 Am^2. They are using CDMA/FDMA, and their operating frequencies are 2450 and 2550 Hz, respectively. The code length is $N = 511$, and the chip rate is $f_{\text{sym}} = 64$ chips/s. RX is equipped with an ARM® Cortex-M4 processor and 16-bit ADC, and contains small triaxial coils (18 mm length, 5 mm diameter, and 25 turns wound on cylindrical ferrite cores) and an IMU for gravity vector estimation. The RX crude noise floor is about -53 dB, but additional signal-to-noise ratio boost is obtained from the CDMA processing gain. The data were recorded from the RX unit via serial port.

Next, the system performance is evaluated in both operation modes. In Section VI-A, we test the network deployment and discovery operation mode, i.e., the single anchor concept, and the joint iterative TX and RX position and orientation refinement algorithm proposed in Section V. The performance of our system operating in user localization mode is evaluated in Section VI-B in terms of RX position and orientation estimation errors. The performance of the ML approach proposed in Section III for fusing position and orientation information from multiple TXs is also compared to the single TX case.

Fig. 11. The two TXs and the RX used in the experiments.

A. Network Deployment and Discovery Operation Mode

In this section, we evaluate the performance of the proposed network deployment and discovery algorithm in Section VI-A, as well as the joint iterative TX-RX position and orientation refinement algorithm proposed in Section V-B. Figs. 12 shows the three phases of the network deployment and discovery algorithm in Section VI-A, for the linear displacement experiment.

Phase I is shown in Fig. 12(b), where the RX 3-D positions and orientations are estimated using TX1 only as an anchor. The hemispherical ambiguity was removed with the basic knowledge that the measured locations are on the positive side of the y-axis of the anchor TX1. The orientation ambiguity was removed based on the gravity vector, which was estimated from the RX inertial measurement unit.

Phase II is depicted in Fig. 12(c), where two estimated RX test locations are used to estimate the position and the orientation of TX2.

Phase III is shown in Fig. 12(d), just before the iterative refinement procedure. The newly discovered anchor TX2 is used to estimate the RX 3-D positions and orientations with the maximum likelihood based fusion algorithm presented in Section III. These TX and RX position and orientation estimates are used to initialize the joint iterative refinement procedure, which will be addressed next. The single anchor approach achieves a maximum 3-D positioning error of approximately 0.7 ms and a maximum orientation error of about 8° for the secondary anchor TX2. These values are going to be further decreased in the iterative procedure.

Fig. 13 shows the results corresponding to the main chamber experiment. Phase III only is shown in Fig 13(b), using the TX positions and orientations determined in the linear displacement experiment. The maximum 3-D positioning error is approximately 2 ms, and will be reduced to less than 1 m after the iterative procedure, as shown next.

1) Iterative TX Position and Orientation Refinement: Fig. 14(a) and Fig. 14(b) show the convergence of the TX2 position and orientation estimates, respectively, using real-world measurements. The algorithm converges in just about 5

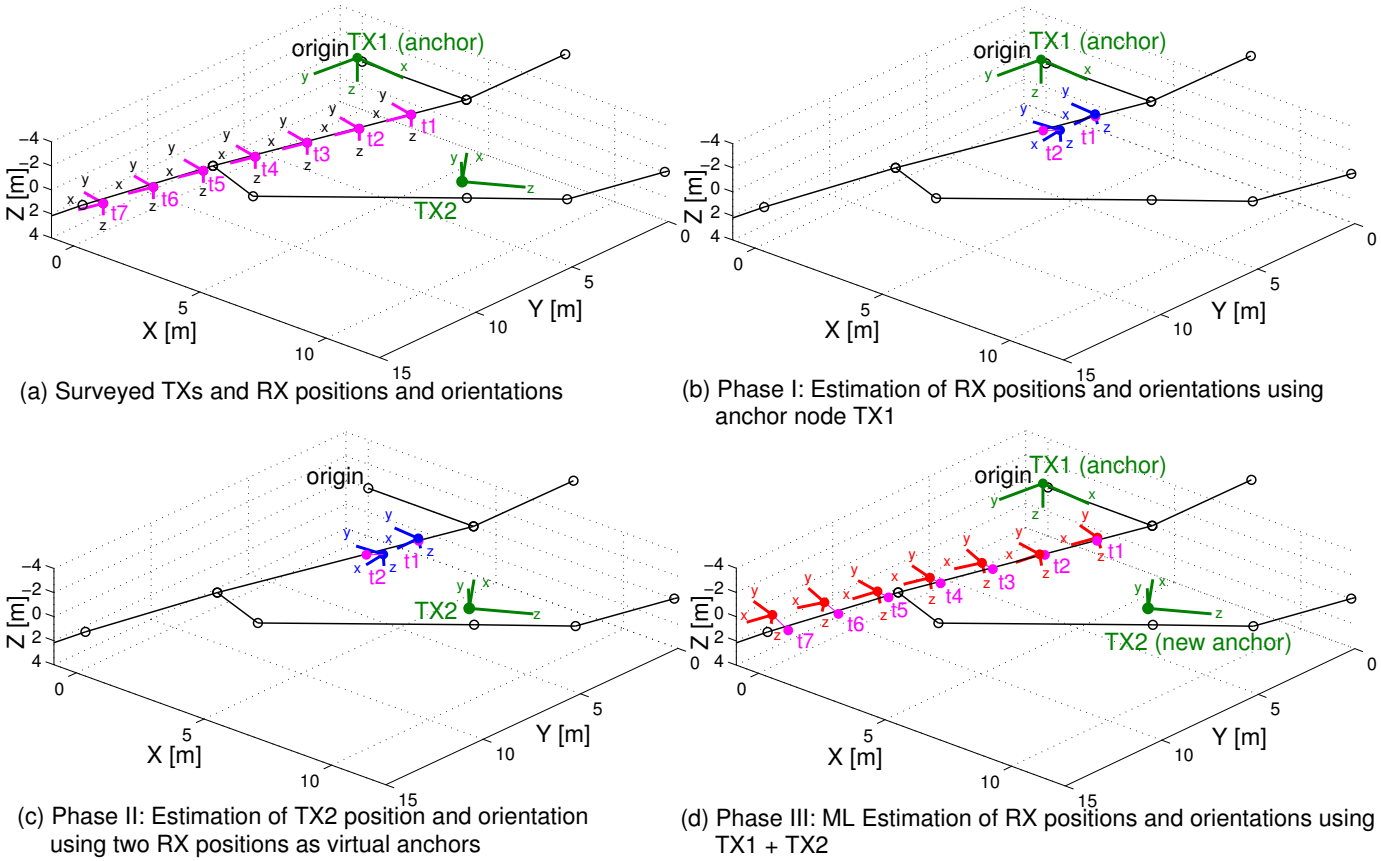

(a) Surveyed TXs and RX positions and orientations

(b) Phase I: Estimation of RX positions and orientations using anchor node TX1

(c) Phase II: Estimation of TX2 position and orientation using two RX positions as virtual anchors

(d) Phase III: ML Estimation of RX positions and orientations using TX1 + TX2

Fig. 12. Linear displacement experiment. The surveyed positions and orientation of TX1 and TX2 are shown in green. (a) Surveyed RX positions and orientations t1–t7 are shown in magenta color. (b) Phase I: Two RX test locations estimated using the single anchor TX1. (c) Phase II: TX2 position and orientation estimation using the previously estimated RX test locations. (d) Phase III: Estimated RX positions and orientations using ML and both TX1 and TX2.

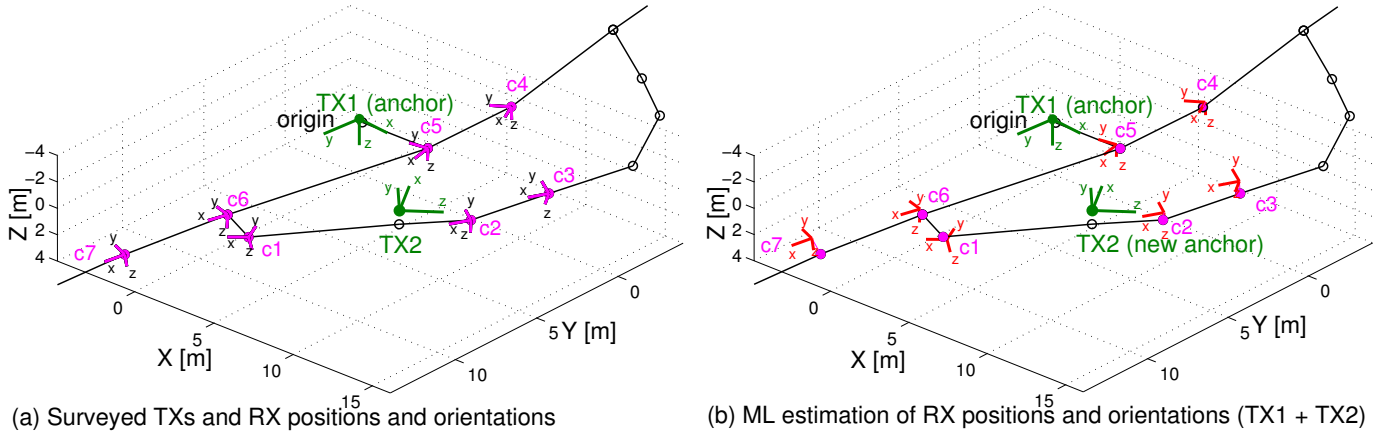

(a) Surveyed TXs and RX positions and orientations

(b) ML estimation of RX positions and orientations (TX1 + TX2)

Fig. 13. Main chamber experiment. The surveyed positions and orientation of TX1 and TX2 are shown in green. (a) Surveyed RX positions and orientations. (b) Estimated RX positions and orientations using ML and both TX1 and TX2.

iterations. The initial TX2 positioning error (the first iteration) achieved by the single anchor approach introduced in Section V-A is already low, around 0.7 ms. After the convergence of the refinement algorithm, the TX2 positioning error stabilizes to approximately 0.4 ms. The TX2 3-D orientation estimation errors shown in Fig. 14(b) are quantified in terms of geodesic distance on $SO(3)$ between the surveyed orientation and the estimated one [given in Eq. (32)]. The initial orientation error is around 8°, whereas the final orientation error is around 5°. We may notice in Fig. 14(b) a slight increase in the TX2 orientation error, and this is because the optimization is done jointly, at the same time, for both TX and RX positions and orientations. Although some position and orientation errors may exhibit a slight increase, the overall TXs and RX position and orientation estimation errors decrease at every iteration.

2) Iterative RX Position and Orientation Refinement: In terms of RX position refinement, the single anchor estimation approach already provides a very reliable initial estimate for most locations, as shown in Fig. 14(c). For the linear displacement experiment (positions `t1` to `t7` shown by black dashed line), the positioning errors are already well below 1 m for most of the locations, as shown in Fig. 14(c). Therefore, the RX positioning errors remain almost the same after the iterative refinement procedure. However, the RX orientation errors decrease significantly, as shown in Fig. 14(d). The initial RX orientation errors range between approximately 4° and 13°, whereas the final errors range between 3° and 9°.

For the the main chamber experiment, the iterative refinement leads to substantial reduction of the RX positioning errors as well, as shown in Fig. 14(c) by the gray solid lines. The initial positioning error ranges between approximately 0.4 and 2 ms, whereas after the algorithm convergence, they range between approximately 0.5 and 0.9 ms.

In Fig. 14(c,d), the initial and the subsequent RX position and orientation estimates correspond to the beginning of Phase III of the network deployment and discovery operation mode. The final errors after convergence correspond to the end of Phase III, when the system ready to operate on user localization mode, which will be addressed next.

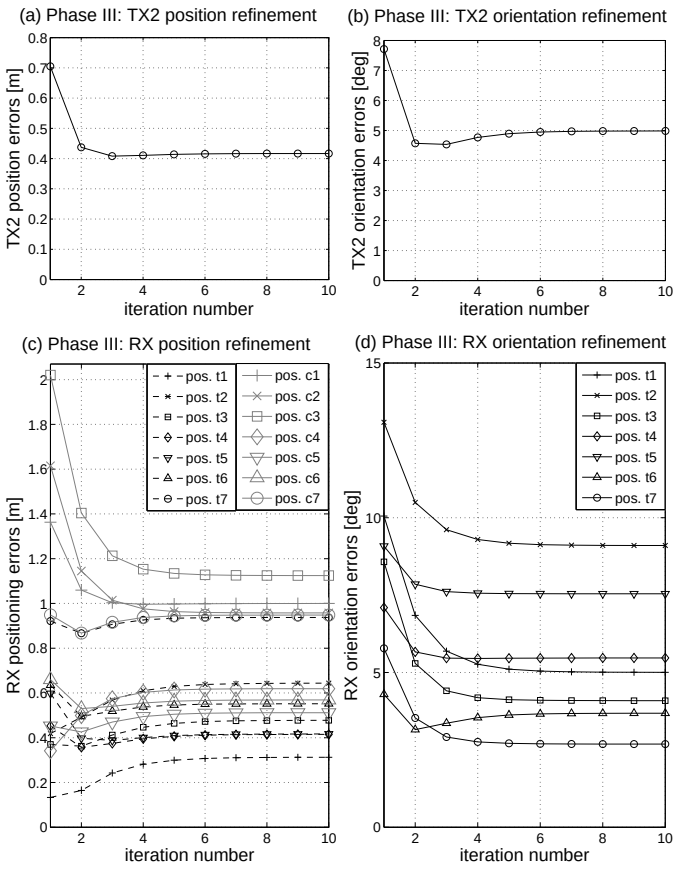

Fig. 14. (a) The single anchor algorithm achieves a low initial TX2 3-D positioning error already, and it is further decreased in the iterative refinement procedure. (b) TX2 3-D orientation error also decreases by few degrees. (c) RX 3-D positioning error exhibits a significant decrease in the main chamber experiment, compared to the initial estimate. (d) The RX 3-D orientation error (shown in terms of geodesic distance) decreases by several degrees for the majority of the locations. Overall the TX and RX position and orientation errors are decreased at every iteration.

B. User Localization Mode

In this section, we evaluate the performance of the proposed localization system operating in user localization mode, in terms of RX position and orientation estimation errors. We also compare the performance of the ML approach proposed in Section III for fusing position and orientation information from multiple TXs to the single TX case.

The system performance in user localization mode is shown by the final values of the RX position and orientation errors in Fig. 14(c) and 14(d), respectively. As shown in Fig. 14(c), submeter accuracy is achieved for all the tested locations whose TX-RX distances range between 4.5 to 15 ms. The orientation estimation errors remain below 10 degrees.

The RX 3-D position and orientation estimation errors from each TX after position and orientation refinement, as well as the ML position estimation error using both TXs are shown in Fig. 15, for each position `t1` to `t7`. RX positioning errors corresponding to the ML algorithm remain below 1 m for all positions measured, as shown by the red line in Fig. 15(a). RX orientation estimation errors also decrease substantially when using the information from two TXs, as shown by the red line in Fig. 15(b). Therefore, fusing 3-D position and orientation information from both TX1 and TX2, improved results are obtained compared to TX1 and TX2 only. Using more than two TXs may further improve the results.

In conclusion, the proposed joint iterative TX-RX position and orientation refinement algorithm shows overall improvement in position and orientation estimates both TX and RX This makes the system suitable for rapid deployment in complex underground landscapes, and ready to operate reliably in user localization mode, which is its ultimate goal.

VII. Related Work

The current underground localization systems typically rely on radio frequency (RF) [1], [3]–[8]. They use either trilateration, multi-dimensional scaling (MDS) [35], or machine learning techniques [3]. A ZigBee anchor-free underground localization method using MDS was proposed in [7], and evaluated using simulations and laboratory experiments. An

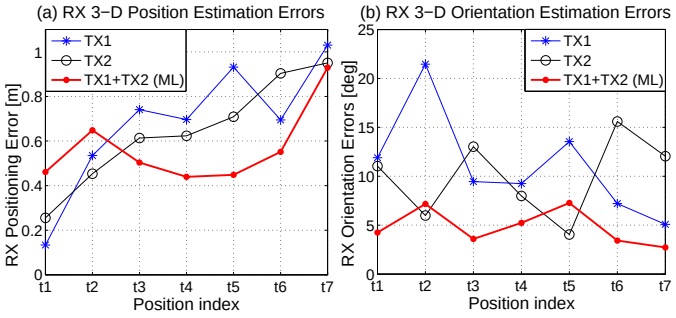

Fig. 15. RX Position (a) and RX orientation (b) estimation errors corresponding to each TX (TX1 – blue curves with star markers, TX2 – black curve with circle markers), as well as both TXs (ML – red curve with dot markers).

underground localization system that uses the rich UWB impulse response features for fingerprinting was introduced in [3], and relies on neural networks. The work in [5] proposes a Hybrid TDOA/RSS underground localization algorithm based on UWB ranging. A UWB-based WSN for monitoring underground coal mines and detecting the structural changes in the event of underground mine collapses was proposed in [4].

Typically, accurate 3-D positioning requires 3-D laser scanners [2], but the device is bulky to carry underground, and prohibitively expensive to be used by teams of workers. To overcome this problem, an automatic position refinement and tracking approach that takes into account the node placement uncertainties was proposed in [6], and it relies on ultra-wideband based round-trip time-of-flight estimation. Time-of-flight provided by special sensor nodes combined with step detection from knee-mounted accelerometer was proposed for underground localization in [36], but only tested in laboratory and simulations. RFID localization to monitor vehicles underground was introduced in [37] using an *a priori* node map, i.e., it is not applicable in unknown environments. A WiFi-based underground localization system using Markov chains was recently proposed in [8], and evaluated in simulations only.

Underground environment poses serious challenges to radio wave propagation [1], [38], hence degrading both the localization accuracy and the communication between nodes. The underground channel propagation characteristics were addressed in [17], [39], and signal propagation techniques for wireless underground communication were proposed in [40], both for RF-based and through-soil magneto-inductive communications. The research challenges for the wireless underground sensor networks such as energy, spatial topology and environment extremes have also been addressed in [38]. The work in [1] addresses the safety assurance and rescue communication systems in mines, and identifies the risks and the challenges for underground safety systems, both in terms of communication and localization. The authors point out the difficulty to set up a ZigBee network in humid, dusty environment, and provide realistic figures. Due to non-line-of-sight (NLOS) conditions, the RF range often did not exceed 15 meters. At lower distances, the packet error rate was worse than 50% for most of the motes, due to channel changes induced by moving personnel, NLOS conditions, and antenna misalignment. Excavations and movement of the mining machinery and people can also radically alter the RF environment resulting into degradation of the localization accuracy and communication disruption. An underground 2-D localization systems that relies on acoustic signals was recently proposed in [41], and its goal is to prevent workers from approaching dangerous mining machinery.

The work in [1] emphasizes that the lack of practical approaches has prevented a robust, generally applicable system, and concludes that the underground networks need a custom design. In this paper, we break up with the traditional underground localization techniques, and propose a magneto-inductive (MI) system that is capable of estimating both the user 3-D position and orientation.

MI 3-D position and orientation estimation using triaxial coils was first proposed by Raab *et al.* in their pioneering paper [42]. For more details on MI-based position and orientation estimation, see also [11], [12], [14], [28], [43]. Our previous work [11] focused on MI indoor localization with additional inertial sensors. Only the single-hop approach was considered, and the positions an orientations of *all* TXs were assumed to be known. Underground magneto-inductive 3-D animal tracking was addressed in [29], [30] using surface antenna loops, but this is restricted to small areas and is not scalable. Reliable through-the-earth communication has been addressed in [17], [24], but did not consider localization. In [44], a numerical MI tracking solution using monoaxial TX coil and triaxial search-coil magnetometer as RX was proposed, but its operation environment is unknown. MI techniques for geophysical prospecting have been addressed in [10]. A cave-to-surface mapping MI system using surface horizontal monoaxial RXs and underground vertical monoaxial TX was introduced in [18]. A "zero-azimuth" underground positioning system was proposed in [19], with TX placed at the surface and the RX underground. Despite being able to operate through various underground media, the methods [18], [19] exploit the geometry of the magnetic field, and therefore, at least three TXs are needed to locate an RX, which increases the infrastructure cost and complexity, or require surveying a large area in order to determine the depth. In the proposed system, all TXs and RXs are placed underground, no survey is required, and two TXs are sufficient to unambiguously solve for the RX 3-D position and orientation.

VIII. Conclusion

In this paper, we propose a underground localization system that uses extremely low frequency magnetic fields. The modulated magnetic signals are appropriate for underground environments, since they do not experience fading, or NLOS attenuation while passing through soil, rock, concrete, water and most natural materials. The proposed system is capable of estimating both 3-D position and orientation of users. It relies on a *single anchor node*, and it is able to automatically discover the spatial topology of the entire network. The infrastructure is made of transmitters that may have completely arbitrarily positions and orientations, as long as the user is

within the coverage area of at least two transmitters, without the need for tedious and expensive underground surveying of anchor positions. A limitation of the current system however is that whilst relative 3-D positioning accuracy is maintained, global positioning errors will accumulate with increasing network depth. This can be addressed either with SLAM based techniques such as loop closure, or with sparse surveying information. Unlike conventional range-based systems, our system imposes no constraints on the geometry of the deployed nodes in order to achieve accurate full 3-D localization, which is a desirable feature in narrow tortuous tunnels. We have shown that increased position and orientation estimation accuracy is achieved by fusing information from multiple anchors. We demonstrated that a network of transmitters was able to maintain accurate 3-D positioning, even through solid rock and obstructions, something which is impossible using conventional RF based technologies.

REFERENCES

[1] P. Misra, S. Kanhere, D. Ostry, and S. Jha, "Safety assurance and rescue communication systems in high-stress environments: A mining case study," *IEEE Communications Magazine*, vol. 48, no. 4, pp. 66–73, Apr. 2010.

[2] GeoSLAM, "ZEB1 3D laser scanning system," details at: http://surveyequipment.com/geoslam-zeb1-3d-laser-scanning-system/.

[3] C. Nerguizian, C. Despins, and S. Affes, "Geolocation in mines with an impulse response fingerprinting technique and neural networks," *IEEE Transactions on Wireless Communications*, vol. 5, pp. 603–611, Mar. 2006.

[4] M. Li and Y. Liu, "Underground coal mine monitoring with wireless sensor networks," *ACM Trans. Sen. Netw.*, vol. 5, no. 2, pp. 10:1–10:29, Apr. 2009.

[5] D. Zhu and K. Yi, "A hybrid TDOA/RSS localization algorithm based on UWB ranging in underground mines," in *Advanced Research on Electronic Commerce, Web Application, and Communication*, ser. Communications in Computer and Information Science, G. Shen and X. Huang, Eds. Springer Berlin Heidelberg, 2011, vol. 144, pp. 402–407.

[6] V. Savic, H. Wymeersch, and E. Larsson, "Simultaneous sensor localization and target tracking in mine tunnels," in *2013 16th International Conference on Information Fusion (FUSION)*, July 2013, pp. 1427–1433.

[7] Z. Pei, Z. Deng, S. Xu, and X. Xu, "Anchor-free localization method for mobile targets in coal mine wireless sensor networks," *Sensors*, vol. 9, no. 4, pp. 2836–2850, 2009.

[8] Y. Guo, H. Liu, L. Shu, and J. Li, "The precise underground localization method based on WiFi network," in *18th Asia-Pacific Conference on Communications (APCC),*, Oct 2012, pp. 664–667.

[9] D. Wang, H. Feng, T. Xing, and J. Sun, "Optimized anchor nodes placement for underground mine localization system based on ZigBee technology," in *Mechatronic Science, Electric Engineering and Computer (MEC), 2011 International Conference on*, Aug 2011, pp. 478–481.

[10] W. M. Telford, L. P. Geldart, and R. E. Sheriff, *Applied Geophysics (2nd edition)*. Cambridge University Press, 1990.

[11] T. E. Abrudan, Z. Xiao, A. Markham, and N. Trigoni, "Distortion rejecting magneto-inductive three-dimensional localization (MagLoc)," *IEEE Journal on Selected Areas in Communications*, vol. 33, no. 11, pp. 2404–2417, Nov. 2015.

[12] G. Pirkl and P. Lukowicz, "Robust, low cost indoor positioning using magnetic resonant coupling," in *ACM International Joint Conference on Pervasive and Ubiquitous Computing (UbiComp 2012)*, Pittsburgh, USA, 2012.

[13] A. Sheinker, B. Ginzburg, N. Salomonski, L. Frumkis, and B. Kaplan, "Localization in 3-D using beacons of low frequency magnetic field," *IEEE Transactions on Instrumentation and Measurement*, vol. 62, no. 12, Dec. 2013.

[14] E. Prigge and J. How, "Signal architecture for a distributed magnetic local positioning system," *IEEE Sensors Journal*, vol. 4, no. 6, pp. 864–873, Dec. 2004.

[15] R. J. Blakely, *Potential Theory in Gravity and Magnetic Applications*. Cambridge University Press, 1996.

[16] R. P. Feynman, R. B. Leighton, and M. Sands, *The Feynman Lectures on Physics*. Addison Wesley, 1964, vol. II.

[17] Z. Sun and I. Akyildiz, "Magnetic induction communications for wireless underground sensor networks," *Antennas and Propagation, IEEE Transactions on*, vol. 58, no. 7, pp. 2426–2435, July 2010.

[18] J. Sogade, Y. Vichabian, A. Vandiver, P. Reppert, D. Coles, and F. Morgan, "Electromagnetic cave-to-surface mapping system," *IEEE Transactions on Geoscience and Remote Sensing*, vol. 42, no. 4, pp. 754–763, April 2004.

[19] C. Davis, W. C. Chew, W. Tucker, and P. Atkins, "A null-field method for estimating underground position," *IEEE Transactions on Geoscience and Remote Sensing*, vol. 46, no. 11, pp. 3731–3738, Nov 2008.

[20] E. C. Jordan and K. G. Balmain, *Electromagnetic Waves and Radiating Systems*. Prentice-Hall, Englewood Cliffs, NJ, 1968, vol. 4.

[21] S. P. Clark Jr., *Handbook of Physical Constants (Revised Edition)*. Yale University, New Haven, Connecticut: The Geological Society of America (Memoir 97), 1966.

[22] J. R. Wait, *Electromagnetic Waves in Stratified Media*. New York: Pergamon, 1971.

[23] O. Kypris, T. E. Abrudan, and A. Markham, "Reducing magneto-inductive positioning errors in a metal-rich indoor environment," in *IEEE Sensors Conference*, 1–4 Nov. 2015, pp. 1–4.

[24] A. Markham and N. Trigoni, "Magneto-inductive networked rescue system (MINERS): taking sensor networks underground," in *"11th International Conference on Information Processing in Sensor Networks (IPSN 2012)*, 2012.

[25] J. I. Agbinya, *Principles of Inductive Near Field Communications for Internet of Things*, ser. River Publishers Series on Communications. River Publishers, 2011.

[26] N. J. Higham, "Matrix nearness problems and applications," in *Applications of Matrix Theory*, M. J. C. Gover and S. Barnett, Eds. Oxford University Press, 1989, pp. 1–27.

[27] M. Costa, V. Koivunen, and H. V. Poor, "Estimating directional statistics using wavefield modeling and mixtures of von-Mises distributions," *IEEE Signal Processing Letters*, vol. 21, no. 12, pp. 1496–1500, Dec. 2014.

[28] J. B. Kuipers, *Quaternions and Rotation Sequences. A Primer with Applications to Orbits, Aerospace, and Virtual Reality*. Princeton University Press, 1999.

[29] A. Markham, N. Trigoni, S. A. Ellwood, and D. W. Macdonald, "Revealing the hidden lives of underground animals using magneto-inductive tracking," in *8th ACM Conference on Embedded Networked Sensor Systems (Sensys 2010)*, Zürich, Switzerland, Nov. 2010.

[30] A. Markham and N. Trigoni, "Underground localization in 3-D using magneto-inductive tracking," *IEEE Sensors Journal*, vol. 12, no. 6, pp. 1809–1816, June 2012.

[31] M. Moakher, "Means and averaging in the group of rotations," *SIAM Journal on Matrix Analysis and Applications*, vol. 24, no. 1, pp. 1–16, 2002.

[32] R. Hartley, J. Trumpf, Yuchao Dai, and Hongdong Li, "Rotation averaging," *International Journal of Computer Vision (Springer)*, vol. 103, no. 3, pp. 267–305, Jul. 2013.

[33] I. Shames, B. Fidan, B. D. O. Anderson, and H. Hmam, "Cooperative self-localization of mobile agents," *IEEE Transactions on Aerospace and Electronic Systems*, vol. 47, no. 3, pp. 1926–1947, 2011.

[34] S. Thrun, W. Burgard, and D. Fox, *Probabilistic Robotics*. Cambridge: The MIT Press, 2005.

[35] J. A. Costa, N. Patwari, and A. O. Hero III, "Distributed weighted-multidimensional scaling," *ACM Transactions on Sensor Networks*, vol. 2, no. 1, pp. 39–64, Feb. 2006.

[36] Y. Yuan, C. Chen, X. Guan, and Q. Yang, "An energy-efficient underground localization system based on heterogeneous wireless networks," *Sensors*, vol. 15, no. 6, p. 12358, 2015.

[37] S. Rusu, M. Hayes, and J. Marshall, "Localization in large-scale underground environments with RFID," in *Electrical and Computer Engineering (CCECE), 2011 24th Canadian Conference on*, May 2011, pp. 001 140–001 143.

[38] I. F. Akyildiz and E. P. Stuntebeck, "Wireless underground sensor networks: Research challenges," *Ad Hoc Net.*, vol. 4, no. 6, 2006.

[39] L. Li, M. C. Vuran, and I. F. Akyildiz, "Characteristics of underground channel for wireless underground sensor networks," in *6th Annual Mediterranean Ad Hoc Networking Workshop*, Corfu, Greece, 2007.

[40] I. F. Akyildiz, Z. Sun, and M. C. Vuran, "Signal propagation techniques for wireless underground communication networks," *Physical Communication*, vol. 2, no. 3, 2009.

[41] R. Pfeil, M. Pichler, S. Schuster, and F. Hammer, "Robust acoustic positioning for safety applications in underground mining," *IEEE Transactions on Instrumentation and Measurement*, vol. PP, no. 99, pp. 1–1, 2015.
[42] F. Raab, E. Blood, T. Steiner, and H. Jones, "Magnetic position and orientation tracking system," *Aerospace and Electronic Systems, IEEE Transactions on*, vol. AES-15, no. 5, Sept. 1979.
[43] Polhemus, "Polhemus Fastrak motion tracking system," URL: http://polhemus.com/motion-tracking/all-trackers/fastrak/.
[44] A. Sheinker, B. Ginzburg, N. Salomonski, L. Frumkis, and B.-Z. Kaplan, "Remote tracking of a magnetic receiver using low frequency beacons," *Measurement Science and Technology*, vol. 25, no. 10, pp. 1–12, 2014.

Traian E. Abrudan (S'02–M'09) received the D.Sc. degree (with honors) from Aalto University, Finland (2008), and the M.Sc. degree from the Technical University of Cluj-Napoca, Romania (2000). During 2010–2013, he was a postdoctoral researcher at the Faculty of Engineering, University of Porto, and a member of Instituto de Telecomunicações, Portugal. Since 2013, he has been a postdoctoral researcher at the Department of Computer Science, University of Oxford, working on practical localization algorithms and systems for humans and robots using low-frequency magnetic fields, as well as other sensing modalities. His fundamental research topics include sensor array signal processing, applied parameter estimation, numerical optimization, and wireless transceiver algorithms.

Zhuoling Xiao (S'14) obtained his PhD degree in Computer Science Department from University of Oxford, in 2015. His research interests focus on sensor networks, including localization, communication and coordination protocols for networked sensor nodes, and machine learning techniques for sensor networks and localization.

Andrew Markham received the Bachelor's (2004) and PhD (2008) degrees in Electrical Engineering from the University of Cape Town, South Africa. He is currently an Associate Professor in the Department of Computer Science, at the University of Oxford, working in the Sensor Networks Group. His research interests include low power sensing, embedded systems and magneto-inductive techniques for positioning and communication.

Dr. Niki Trigoni is a Full Professor at the Department of Computer Science, University of Oxford. She obtained her PhD at the University of Cambridge (2001), became a postdoctoral researcher at Cornell University (2002-2004), and a Lecturer at Birkbeck College (2004-2007). Since she moved to Oxford in 2007, she established the Sensor Networks Group, and has conducted research in communication, localization and in-network processing algorithms for sensor networks. Her recent and ongoing projects span a wide variety of sensor networks applications, including indoor/underground localization, wildlife sensing, road traffic monitoring, autonomous (aerial and ground) vehicles, and sensor networks for industrial processes.